Advanced tokamak profile evolution in DIII-D

M. Murakami,[a] M.R. Wade,[a] J.C. DeBoo,[b] C.M. Greenfield,[b] T.C. Luce,[b] M.A. Makowski,[c] C.C. Petty,[b] G.M. Staebler,[b] T.S. Taylor,[b] M.E. Austin,[d] D.R. Baker,[b] R.V. Budny,[e] K.H. Burrell,[b] T.A. Casper,[c] M. Choi,[b] J.R. Ferron,[b] A.M. Garofalo,[f] I.A. Gorelov,[b] R.J. Groebner,[b] R. La Haye,[b] A.W. Hyatt,[b] R.J. Jayakumar,[c] K. Kajiwara,[b] J.E. Kinsey,[g] L.L. Lao,[b] J. Lohr,[b] D. McCune,[e] R.I. Pinsker,[b] P.A. Politzer,[b] R. Prater,[b] H.E. St. John,[b] and W.P. West[b]

[a]*Oak Ridge National Laboratory, Oak Ridge, Tennessee, 37831 USA*
email: murakami@fusion.gat.com

[b]*General Atomics, P.O. Box 85608, San Diego, California, 92186-5608 USA*

[c]*Lawrence Livermore National Laboratory, Livermore, California 94551 USA*

[d]*University of Texas, Austin, Texas.*

[e]*Princeton Plasma Physics Laboratory, Princeton, New Jersy 08543 USA*

[e]*Princeton Plasma Physics Laboratory, Princeton, New Jersy 08543 USA*

[f]*Columbia University, New York, New York USA*

[g]*Lehigh University, Bethlehem, Pennsylvania 18015 USA*

Abstract. Using off-axis electron cyclotron current drive (ECCD), self-consistent integrated advanced tokamak operation has been demonstrated on DIII-D combining high β (>3%) at high q ($q_{min} > 2.0$)

with good energy confinement (H_{89} ~ 2.5) and high noninductive current fraction (f_{BS} ~ 55%, f_{NI} ~ 90%). Modification of the current profile by ECCD led to internal transport barrier formation even in the presence of type I edge localized modes. Improvements were observed in all transport channels, and increased peaking of profiles led to higher bootstrap current in the core. Separate experiments have shown the ability to maintain a nearly steady-state current profile for up to 1 s with $q_{min} > 1.5$. Modeling indicates that this favorable current profile can be maintained indefinitely at a higher β_N using tools available to the near-term DIII-D program. Modeling and simulation have become essential tools for the experimental program in interpreting the data and developing detail plans for new experiments.

PACS Nos. 52.65, 52.55F, 52.50.Gj, 52.55Pi

I. INTRODUCTION

The attractiveness of any fusion power system relies heavily on providing high power density and high duty factor (or steady state) [1,2]. The DIII-D Advanced Tokamak (AT) program is aimed at developing the physics basis and plasma control methods needed for steady state high performance operation. Steady-state operation requires that the plasma current be driven noninductively. High bootstrap current [3] is desired to minimize the recirculating power. The achievement of a self-consistent solution that combines high bootstrap current fraction and high fusion gain requires moderately high safety factor (q) and high values of normalized beta (β_N). Both experimental experience and simulations suggest that a relatively small (~10%) amount of current driven at about the half radius, combined with bootstrap and neutral beam current drive (NBCD), can result in a steady state current profile that is compatible with a high β equilibrium.

Recent experiments [4,5] on DIII-D have demonstrated off-axis electron cyclotron current drive (ECCD) [6] as an effective tool to control the current profile in Advanced Tokamak operation with the following characteristics: high β operation at high q_{min}, good plasma confinement and good current drive efficiency. Utilizing off-axis ($\rho = 0.4$) ECCD to modify the current density profile in a plasma operating above the no-wall ideal stability limit with $q_{min} > 2.0$, plasma conditions with $\beta \sim 3\%$ and the noninductive current fraction of ~90% were produced and sustained for nearly 2 s (limited only by the duration of the ECCD pulse). This experiment successfully integrated all of these elements simultaneously. In these discharges, ECCD is essential to producing negative central magnetic shear, helping to form a weak internal transport barrier (for both ions and electrons) that is maintained in the presence of a fully developed H-mode edge with type I edge localized modes (ELMs).

Modeling and simulation have become essential tools for this experimental program. Modeling prior to the experiment based on an existing DIII-D discharge was used to develop detailed experimental plans. Figure 1 shows the temporal evolution of the safety factor and current profile predicted by modeling prior to the experiment based on a target discharge with neutral beam injection (NBI) only. Upon application of 3 MW ECCD localized at $\rho = 0.4$, the central magnetic shear is predicted to become negative, primarily due to an increase in q_0. The $q_{\min}$ value is predicted to transiently decrease, but evntually become stationary at higher levels than in the NBI-only reference discharge. ECCD is predicted to prevent continuous inward penetration of Ohmic current and to sustain the required off-axis current peak position. The modeling successfully predicted the features of experimental results, and helped bring theory, experiment and diagnostics together in the execution and analysis of these experiments. Predictive modeling indicates that fully noninductive sustainment of high β discharges is possible with tools available to the near term DIII-D program.

In this paper, we describe an overview of the discharge evolution with ECCD, and compare it with similar discharges with electron cyclotron heating (ECH) [no current drive (CD)] and NBI-only. We then discuss ECCD analysis and current profile evolution. Results of a 1-1/2 D transport calculation of current profile evolution are compared with key experimental measurements such as motional Stark effect (MSE) diagnostics and internal loop voltage analysis. We then discuss a separate experiment where nearly steady state current and pressure profile at high β were maintained with $q_{min} > 1.5$. Finally, we use this discharge as a basis for predictive modeling for fully noninductive operation with broadly distributed off-axis ECCD at a higher β.

II. EXPERIMENT IN THE $q_{min} > 2$ REGIME

Figure 2 compares three AT discharges with similar operational parameters: a reference shot with NBI alone; one with ECCD; and the other with ECH (electron cyclotron heating; no CD). In these discharges, H-mode was induced early in the current ramp to slow down the penetration of the Ohmic current giving high q_{min}, $q_{min} > 2.5$, at the end of the current ramp. After β_N was ramped up, feedback control of the neutral beam power was used to maintain $\beta_N = 2.8$. This value was above the measured no-wall stability limit ($\beta_N \sim 2.5$) and was below the experimental β limit ($\beta_N \sim 3.2$) under the discharge conditions. The discharge maintained H-mode with fully developed Type-I ELMs with confinement improvement factor, $H_{89} = 2.4$. Density control was achieved with divertor pumping by slightly unbalancing a double-null divertor discharge with the ∇B drift toward the upper, pumped divertor. Strong pumping maintained a line-average density of $\sim 3.4 \times 10^{19}$ m^{-3} with low pedestal density. Effective atomic charge (Z_{eff}) was below 2 in the core with a minimal contribution of metal impurities ($\Delta Z_{eff} < 0.1$). Approximately 2.5 MW of EC power (absorbed) from five 110-GHz gyrotrons was applied at 1.5 s (0.2 s after the start of the high-β phase) and continued for a duration of up to 2 s [7]. In the ECCD case, the waves were launched at an oblique angle with respect to the major radius to generate current parallel to the plasma current. In the ECH case, EC power was injected radially with no current drive. With use of a moveable mirror, the EC beams are directed to damp in a narrow region near $\rho \sim 0.5$ on the inboard side of the magnetic axis, in both cases. Upon application of ECCD, changes in the magnetic configuration were evident in the q profile evolution [Fig. 2(d)], as predicted by the modeling prior to the experiment [Fig. 1(a)]. A significant increase in negative central shear was observed within 0.5 s of the start of ECCD and then maintained for the duration of the ECCD pulse with q_0 increasing to ~5 while q_{min} remained above 2. The current profile modification was due to current drive, rather than

to heating, since the q evolution for the ECH case was nearly identical to that with NBI alone. Performance improvement in the core as shown by increases in central T_i and T_e was observed only with ECCD.

The measured ECCD efficiency is consistent with theoretical predictions and that required for an advanced tokamak target scenario. The analysis of the driven current based on a technique [8] of examining the difference of pitch angles, measured by the MSE diagnostic [9], between the ECCD discharge and those without CD (ECH or similar NBI-only discharges) gives an ECCD estimate of 130±36 kA. This value agrees well with a prediction of 120 kA from a quasi-linear Fokker-Planck code, CQL3D [10]. The high CD value was due to successful plasma density control (for high T_e), and the reduction of trapped electron effects resulting from: (a) EC absorption on the inboard side, and (b) high electron beta which moves the resonance location away from the trapping boundary in velocity space [11]. The driven current value corresponds to a normalized CD efficiency, $\zeta = 33\, n_{20} I_A R_m/(P_W T_{kev}) = 0.26$. This is encouraging in that we have achieved sufficient normalized ECCD efficiency to carry out our planned AT program in the coming years.

To understand the complex interaction between ECCD and the other current sources in improving tokamak operation and maintaining the current density profile, simulations of the magnetic equilibrium evolution are conducted with a 1-1/2 D transport code, TRANSP [12]. The transport code steps forward in time and evolves the poloidal magnetic field and parallel electric field with a plasma boundary fixed to an experimental shape at 20 ms before the start of ECCD/ECH. Experimental plasma profiles (T_e, T_i, n_e and Ω_{tor} as shown in Fig. 3 and Z_{eff}) are input to the code every 25 ms. The equilibrium is calculated at intervals of 10 ms. Three noninductive current sources are involved: ECCD, NBCD, and bootstrap current. The electron cyclotron driven current and heating power to electrons are calculated by a linear ray tracing code

TORAY-GA [13] running within a transport code ONETWO [14]. The CD values calculated by TORAY-GA are multiplied by a factor of 1.2 to agree with values from CQL3D [10]. NBCD is calculated by TRANSP with a Monte-Carlo slowing down calculation. A modest amount of anomalous fast ion spatial diffusion (0.3 m^2/s) is assumed in order to match the measured neutron rate and plasma stored energy. This approximates the effect of Alfvén modes and is usually consistent with DIII-D analysis in a wide range of confinement regimes. Inclusion of anomalous diffusion decreases the calculated on-axis beam driven current by ~40% and the total NBCD by ~15% [15]. Bootstrap current is calculated by the Hirshman 78 model with the large aspect ratio approximation [16], because the 1997 NCLASS [17] model that is available in TRANSP had numerical stability problems for certain DIII–D shots. The Hirshman 78 model has been compared with two leading bootstrap current models: latest NCLASS model [17] and Sauter model [18]. The effects of different approximations to collisionality and geometry are found to be less than 10% of the total bootstrap current under the present experimental conditions.

The profiles of the total current calculated from this procedure (Fig. 4) shows that ECCD prevents inward Ohmic current penetration. The noninductive current density clearly peaks off-axis. As the density peaking increases, the bootstrap current increases inside the ECCD radius, which broadens the local peak of J_ϕ at $\rho \leq 0.4$. Nevertheless, the peak current density position remains robustly fixed at $\rho = 0.4$, as long as the ECCD continues. This was not the situation in the ECH case, where the current peak continues to move in, as indicated by the broad peak of J_ϕ.

The current profile evolution predicted by the simulation can be directly compared with the MSE polarimetry. The measured pitch angles depend not only on the poloidal magnetic field (B_θ), but also on the radial electric field (E_r). Although the MSE measurements can determine E_r as well as B_θ due to different viewing directions [9], we

supply the E_r information from charge exchange recombination (CER) measurements for carbon impurity:

$$E_r = (Z_i e n_i)^{-1} \nabla p_i - v_{\theta i} B_\phi + v_{\phi i} B_\theta$$

where Z_i is the ion charge, n_i is the ion density, e is electric charge, P_i is the ion pressure and v_θ and v_ϕ are the poloidal and toroidal rotation velocities. With strong tangential NBI, E_r in the core (typically up to ~50 keV/m) is dominated by the toroidal flow. In the MSE analysis and simulations, systematic offsets errors in the calibration in individual channels were adjusted to agree with calculated pitch angles (including E_r effects) at one early time (t = 1.4 s for the ECCD case). MSE simulations with E_r effects included reproduces the MSE signals throughout the discharges extremely well [4]. This includes fluctuations due to varying plasma conditions (e.g., due to ELMs) and E_r variations introduced by the NBI power feedback.

Figure 5 shows good agreement between experiment and simulation in the local toroidal component of the plasma current as a function of the midplane major radius for ECCD and ECH. The experimental local current density (J_ϕ) is obtained from measured B_θ along the midplane using Ampere's law and the closed magnetic field line properties as discussed in Ref. [19]. The experimental J_ϕ for each case is shown by three different histograms corresponding to three different MSE systems: tangential, radial, and edge. Both the simulation and the MSE measurements show broad current profile with ECH and more off-axis peaked with ECCD. The off-axis peak is broader than the ECCD driven current. This is because: (1) substantial Phirsch-Schlüter current component which is averaged out once it is flux-surface averaged; and (2) bootstrap current aligned to the inboard side of the ECCD current peak.

Figure 6(a) shows the flux-surface averaged toroidal current components and comparison of the Ohmic current component with the experimental Ohmic current measurement. The experimental Ohmic current is obtained from an internal loop voltage analysis [20] using a time series of reconstructed equilibria based on magnetic and MSE measurements with kinetic pressure inputs. The simulated Ohmic current agrees well with the experimental Ohmic current profile. Based on the internal loop voltage analysis, the noninductive current fraction is ~90%. The noninductive current fraction from the simulation is about 85%, which is maintained for the duration of ECCD, as shown in Fig. 6(b). As discussed earlier, the Sauter bootstrap model and NCLASS model agree with the Hirshman model [16] to ±5%. The simulation result is consistent with the loop voltage analysis.

Improvement in bootstrap current arises from increased peaking of density and temperature profiles. The off-axis electron temperature was increased by the off-axis heating for ECCD and ECH cases, but an increase in the central electron temperature was only evident with ECCD, as seen in Fig. 2(f) and the radial profile in Fig. 3(b). The central ion temperature increased substantially with ECCD. The performance improvement observed in this case is in contrast to typical observations of significant confinement deterioration when electron heating is applied in plasmas with $T_i >> T_e$ [21,22]. ECCD was essential to producing negative central shear (NCS) and forming a weak ITB (in both electrons and ions) that was maintained in the presence of Type-I ELMs. Since the primary difference between the ECCD case and the ECH [and also neutral beam injection (NBI)-only] case was the change of the current density profile, the improved transport properties are the direct consequence of the change in the current profile, i.e., the increase in NCS induced by the ECCD.

Improved transport was observed in all transport channels, as shown by electron thermal, ion thermal, electron particle, and toroidal momentum diffusivities

[Fig. 7(a)–(d)] based on power balance analysis using TRANSP. The electron diffusivity, χ_e, suddenly increases in the ECCD/ECH power deposition region which is the shear reversal region. That itself is the effect of off-axis heating, and not necessarily related to shear reversal. This adjustment in χ_e is necessary in order to avoid hollow temperature profiles during off-axis electron heating. However, the reduction in χ_e to a level below the NBI-only case is observed only in the ECCD case, but not ECH case. Figure 7(b) shows comparison of the effective ion thermal diffusivity (i.e., both conductive and convective heat transport included) and the effective neoclassical ion diffusivity. The experimental χ_i^{eff} value is nearly equal to the neoclassical χ_i^{neo} value in the core region ($\rho < 0.35$) in the ECCD case, but much larger than χ_i^{neo} at outer radii.

The confinement improvement with ECCD, is evaluated using the gyrokinetic stability (GKS) code [23], which calculates the stability of ion temperature gradient (ITG) modes. Figure 8(a) compares the measured $a/L_{T_i} = -a\,(dT_i/dr)/T_i$ and the minimum value of $a/L_{T_{i,crit}}$ needed for ITG mode instability, showing that the experimental a/L_{T_i} is in general comparable to the ITG mode critical value for the ECH case [Fig. 8(a)]. This indicates that ITG modes may be limiting the T_i profile. With ECCD [Fig. 8(b)], however, the stronger NCS and α-stabilization (and E×B flow shear) are expected to stabilize ITG modes. Our initial puzzle was why then a/L_{T_i} for this case does not go up to the critical value for ITG modes. The local stability criterion (D_R) for resistive interchange modes [24] has been evaluated, [Fig. 8(b)], indicating that the core region ($\rho = 0.15$–0.41) for the ECCD (but not ECH) discharge is unstable ($D_R > 0$) to resistive interchange modes (indeed, there were a few low amplitude MHD bursts observed in Mirnov signals). Since the GKS code uses the ballooning representation and cannot resolve interchange modes, the GKS code calculation is invalid in this region [25]. It is also pointed out that the effective neoclassical thermal diffusivity becomes nearly equal to the experimental value at $\rho < 0.35$ for the ECCD case [Fig. 8(b)], as discussed earlier.

III. EXPERIMENT IN THE $q_{min} > 1.5$ REGIME

Although the $q_{min} > 2$ regime has an advantage of minimizing susceptibility to neoclassical tearing modes (NTMs), the experimentally attainable β_N values are found to be lower than that in the $2 > q_{min} > 1.5$ regime. The maximum achievable beta in the experiment and the measured no-wall, ideal n = 1 limit decrease with increasing q_{min}[26]. β_N values of 3.5–4.0 have so far been possible only with $q_{min} < 2$. These β_N values are significantly above the no-wall beta limit and robust operation has been made possible by resistive wall mode (RWM) stabilization. With suitably broad pressure profiles and wall stabilization, stability calculations indicate that high beta at high q_{min} should be possible.

Utilizing a $2 > q_{min} > 1.5$ target discharge, ECCD has been used to sustain a steady current density profile for up to 1.0 s. Figure 9 shows time histories of the discharge with ECCD. The early H-mode technique was used as before, but the high power phase was delayed until q_{min} dropped below 2.0. NBI feedback was used to maintain $\beta_N \sim 3.1$, corresponding to $\beta \sim 3.3\%$ with $H_{89} \sim 2.4$. The configuration with q_0 above 2.0 and q_{min} below 2.0 was maintained for 1.0 s with 2 MW of off-axis ECCD. The duration of the configuration was limited by the onset of small m=5/n=3 NTMs as q_{min} continued to evolve slowly. Both the q profile and J profile are stationary for the first second of ECCD. J_ϕ from MSE and a simulation agreed well, indicating that the current profile was stationary. The OH current density profile is in reasonable agreement with that from simulation. A noninductive current fraction of ~85% was obtained in this $q_{min} > 1.5$ regime.

IV. PREDICTIVE MODELING FOR FULL NONINDUCTIVE OPERATION

An NBI discharge with $\beta_N \sim 4$ has been obtained with $q_{min} \sim 1.5$. In this discharge, $\beta_N H_{89} > 10$ was maintained for a period of $4\tau_E$ with minimal MHD activity [27]. Predictive modeling was carried out based on one of these high-β_N NBI target discharges with $q_{min} \sim 1.5$. Results of the modeling are shown in Fig. 10. The modeling indicates that 3.5 MW of broadly distributed, off-axis, ECCD can achieve full noninductive operation with $\beta_N = 4.0$, $H_{89} = 3.1$ and $f_{BS} = 0.65$. Sustaining this high β_N value requires reliable RWM stabilization that we are still developing. In the near-term we try to extend the existing $q_{min} > 1.5$ discharge to be fully noninductive, while maintaining some stability margin. A predictive simulation was carried out to show what is required to achieve this goal.

In the predictive simulation [28], we used transport coefficients [$\chi_e(\rho)$ and $\chi_i(\rho)$] calculated from the existing ECCD discharge with $q_{min} > 1.5$, and validated the transport coefficients with the experimental profiles (T_e, T_i, and j). We then increased the β_N value by raising the NBI power by 4 MW, and multiplied the transport coefficients by a degradation factor based on H98y2 scaling relation ($\chi \propto P^{0.69}$) [29]. Figure 11 shows results of the predictive modeling along with those from the existing ECCD shot, indicating that full noninductive operation is possible using broadly distributed, off-axis, 2.5 MW ECCD at slightly higher β_N. The β_N values shown for the existing shot and the prediction are from kinetic analysis. We observed that magnetically measured β_N values are about 10% higher than the kinetic β_N values on which the predictive simulations are based. Even with the pessimistic transport coefficient (χ) and the pessimistic power law scaling used, the necessary NBI power (13 MW) is well within the DIII-D NBI capability. Therefore the requirements suggested by the simulation are likely an overestimate of the actual requirements. The ECCD capability expected in 2003 includes a 4 s duration of ECCD at $P_{EC} \sim 2.5$ MW. This indicates that fully noninductive

sustainment of the high β discharge for about one current replacement time (τ_{CR}) is possible with tools available in the near term.

V. CONCLUSION

In conclusion, the current profile has been modified using off-axis ECCD with $q_{min} > 2$ at high β. Strong negative central shear was produced. Reduction of transport coefficients were observed in all transport channels. A bootstrap fraction of 55% and noninductive current fraction of ~90% were achieved. Higher values have been limited by attainable β_N. In separate experiments, the current profile has been sustained with $q_{min} > 1.5$ at higher β. Nearly steady-state current and pressure profiles were maintained for 1 s. Good access to this regime was demonstrated where higher f_{BS} values are possible with higher β_N. Predictive modeling was validated for full noninductive operation with $q_{min} > 1.5$ with tools available in the near term.

These results have demonstrated the role of simulations in optimization of Advanced Tokamak experiments. Experiments based on these simulations have demonstrated plasma conditions that self-consistently integrate the key ingredients of Advanced Tokamak: high bootstrap current fraction, high beta, and good confinement. In addition, ECCD has been validated as an efficient, localized, current profile control tool in high beta plasmas. Integrated modeling and simulation was key to the experimental success and we believe heralds a new era of the use of modeling and computing to guide experimental efforts in fusion plasmas.

Acknowledgment

This work was supported by the U.S. Department of Energy under Contract Nos. DE-AC05-00OR22725, DE-AC03-99ER54463, W-7405-ENG-48, and DE-AC02-76CH03073 and Grant Nos. DE-FG03-97ER54415 and DE-FG02-92ER54141. We would like to thank the DIII-D Team, in particular, the ECH Group for successfully carrying out these experiments. We also wish to acknowledge useful discussions with W.A. Houlberg. The modeling was carried out using Grid-enabled TRANSP on the National Fusion Grid, and we would like to thank the members of the National Fusion Collaboratory Project (www.fusiongrid.org) sponsored by the US DOE SciDAC Program.

References

[1]F. Najmabadi *et al.*, Fusion Energy 2000 (Proc. 18th Int. Conf., Sorrento, 2000), (IAEA, Vienna, 2001) CD-ROM, File FTP 2/15 and http://www.iaea.org.programmes/ripc/physics/fec2000/html/node1.htm.

[2]T.S. Taylor, Plasma Phys. and Control. Fusion **39**, B47 (1997).

[3]R.J. Bickerton, *et al.*, Nature (Phys. Sci.) **229**, 110 (1971).

[4]M. Murakami, *et al.*, "Modification of the Current Profile in High Performance Plasmas Using Off-Axis Electron Cyclotron Current Drive in DIII-D," submitted to Phys. Rev. Lett. (2002).

[5]M.R. Wade, *et al.*, "Title," in Proc. of the 2002 IAEA Fusion Energy Conf., Lyon, France, and to be published in Nucl. Fusion (2002).

[6]N. Fisch, Rev. Mod. Phys. **59**, 175 (1987).

[7]J. Lohr, Yu. Gorelov, R.W. Callis, *et al.*, "High Power Long Pulse Operation of the DIII-D Gyrotron Installation," Proc of the 12th Joint Workshop on Electron Cyclotron Emission and Electron Cyclotron Heating, G. Giruzzi ed., CEA-Cadarache, France (2002).

[8]C.C. Petty, *et al.*, Nucl. Fusion **41**, 551 (2001).

[9]B.W. Rice, *et al.*, Phys. Rev. Lett. **79**, 2694 (1997).

[10]R.W. Harvey and M.C. McCoy, Proc. IAEA Tech. Comm. Mtg. on Advances in Theory and Modeling of Thermonuclear Plasmas, Montreal, 1992 (IAEA, Vienna, 1993) p. 498.

[11]R. Prater, *et al.*, Radio Frequency Power in Plasmas, (Proc. of the 14th Topical Conf., 2001) Edited by T.K. Mau and J.S. deGrassie, AIP Conf. Proc. No. 595 (AIP, New York, 2001) p. 302.

[12]R.J. Hawryluk, *et al.*, Physics Close to Thermonuclear Conditions, Vol. 1 (Commission of the European Communities, Brussels, 1980) p. 19.

[13]K. Matsuda, IEEE Trans. Plasma Sci. **17**, 6 (1989).

[14]H.E. St. John, *et al.*, Plasma Phys. and Control. Nucl. Fusion Research 1994 (Proc. of the 15th IAEA Conf., Seville, 1994) Vol. 3 (IAEA, Vienna, 1994) p. 603.

[15]H.E. St. John, *et al.*, in Controlled Fusion and Plasma Physics (Proc. 28th Euro. Conf., Madeira, 2001) paper P5.037; also General Atomics Reort GA-A23721 (2001).

[16]S.P. Hirshman, Nucl. Fusion **18**, 917 (1978).

[17]W.A. Houlberg, *et al.*, Phys. Plasmas **4**, 3230 (1997).

[18]O. Sauter, *et al.*, Phys. Plasmas **6**, 2834 (1999)

[19]C.C. Petty, *et al.*, Nucl. Fusion **42**, 1124 (2002).

[20]C.B. Forest, *et al.*, Phys. Rev. Lett. **73**, 2244 (1994).

[21]C.M. Greenfield, *et al.*, Nucl. Fusion **39**, 1723 (1999).

[22]C.C. Petty, *et al.*, Phys. Rev. Lett. **83**, 3661 (1999).

[23]M. Kotschenreuther, *et al.*, Comp. Phys. Comm. **88**, 128 (1995); and also R.L. Miller, et al., Phys. Plasmas **5**, 973 (1998).

[24]J.M. Greene and M.S. Chance, Nucl. Fusion **21**, 453 (1981).

[25]G.M. Staebler, *et al.*, Plasma Phys. and Control. Nucl. Fusion Research 1999 (Proc. of the 17th IAEA Conf., Yokohama, 1998) Vol. ?? (IAEA, Vienna, 1998) p. ??. also General Atomics Report GA-A22988.

[26]J.R. Ferron, *et al.*, "Progress Toward Sustained High-Performance Advanced Tokamak Discharges in DIII-D," in the Proc. of the 29th Euro. Conf. on Plasma Physics and Controlled Fusion, Montreux, Switzerland, 2002 (European Physical Society, 2002).

[27]M.R. Wade, *et al.*, "Physics of High Bootstrap Fraction, High Performance Plasmas on the DIII-D Tokamak," in the Proc. of 28th EPS Conf. on Controlled Fusion and Plasma Physics, Madeira, Portugal, 2001 (European Physical Society, 2002).

[28]M. Murakami, *et al.*, Nucl. Fusion **40**, 1257 (2000).

[29]ITER Physics Basis, Nucl. Fusion **39**, 2208 (1999).

List of Figure Captions

Fig. 1. (a) Temporal evolution of central safety factor, q_0, and minimum safety factor, q_{min}, and (b) profiles of total safety factor current profile predicted prior to the experiment using localized 3 MW ECCD (red traces), compared with an existing NBI only (black curve) discharge.

Fig. 2. Comparison of temporal evolution of parameters for three discharges: reference shot with NBI alone (black), ECCD (red) and ECH (green) in the $q_{min} > 2$ regime; (a) plasma current, neutral beam power (smoothed (±40 ms box-car), feedback modulated to maintain constant β, and EC power; (b) line-averaged electron density, and $D\alpha$ signals; (c) normalized beta and 4 times internal inductance; (d) central q (dash) and minimum q (solid) values; (e) ion temperature at $\rho \approx 0.1$ and 0.4 from CER diagnostic; and (f) electron temperature from ECE at $\rho \approx 0.1$ and 0.4.

Fig. 3. Radial profiles of (a) safety factor, (b) ion and electron temperature, (c) electron density (d) toroidal angular velocity for discharges with ECCD (bold) and ECH (fine). The error bars are one standard deviation of 16 profiles over 400 ms. The shaded area is the region of NCS for the ECCD discharge.

Fig. 4. Evolution of the total plasma current density profile for discharges with ECCD (bold) and ECH (fine).

Fig. 5. Local toroidal current density derived from MSE pitch angle measurements (histogram) and calculated from the simulation (continuous line) for discharges with ECCD (bold) and ECH (fine) at 2.5 s with a time average of ±50 ms. J_{ECCD} calculated by the quasi-linear CQL3D code is also shown. Three different histograms for each

discharge correspond to three different views of the MSE diagnostic systems: tangential (solid), radial (dash) and edge (chain).

Fig. 6. (a) Toroidal current density components, neutral beam CD, ECCD, bootstrap, and Ohmic current at t = 2.5 s, and (b) evolution of noninductive current fractions for the discharge with ECCD. Bootstrap current calculated using Hirshman 78 model. The Ohmic current profile from the experiment (internal loop voltage analysis) is shown with hatched area. The Ohmic current fraction based on the measurement is shown in (b).

Fig. 7. Radial profiles of (a) electron thermal diffusivity, (b) effectie ion thermal diffusivity and effective ion neoclassical diffusivity, (c) electron particle diffusivity, and (d) toroidal momentum diffusivity for discharges with ECCD (bold) and ECH (fine) from power balance analysis. The error bars are one standard deviation of 40 profiles spanning over 400 ms. The shaded area is the region of negative central shear for the ECCD discharge.

Fig. 8. Profiles of measured normalized ion temperature gradient scale length (a/L_{T_i}) and computed critical a/L_{T_i} value for ion temperature gradient (ITG) mode instability for (a) the ECH case, and (b) the ECCD case. Also shown in the computed resistive interchange stability parameter D_R which is unstable (>0) only for the ECCD case.

Fig. 9. Comparison of temporal evolution of parameters for discharges in the $q_{min} > 1.5$ regime, (a) plasma current, neutral beam power (smoothed for feedback modulated power), and EC power; (b) normalized beta and 4 times internal inductance; (c) central and minimum q values; (d) central ion and electron temperature; and (5) magnetic fluctuations of odd toroidal number (whose primary component was identified as n = 3).

Fig. 10. Predictive modeling of 3.5 MW broadly distributed ECCD in a high β_N q_{min} ~ 1.5 discharge: (a) evolution of safety factor profile, (b) initial and final (20 s) electron and ion temperature, and (c) current components. Modeling indicates that full noninductive operation is possible with parameters of $\beta_N = 4.0$, $H_{89} = 3.1$ and $f_{BS} = 0.65$.

Fig. 11. Predictive simulation for full noninductive operation compared with the experiment in the $q_{min} > 1.5$ regime. (a) Noninductive current fractions, (b) normalized beta which is still below the maximum β_N observed, (c) profile of safety factor, remaining nearly stationary at the experimental level (t = 3.8 s) throughout the simulation period, and (d) profiles of noninductive current sources and Ohmic current. Negative Ohmic current implies that the system is overdriven with noninductive current sources.

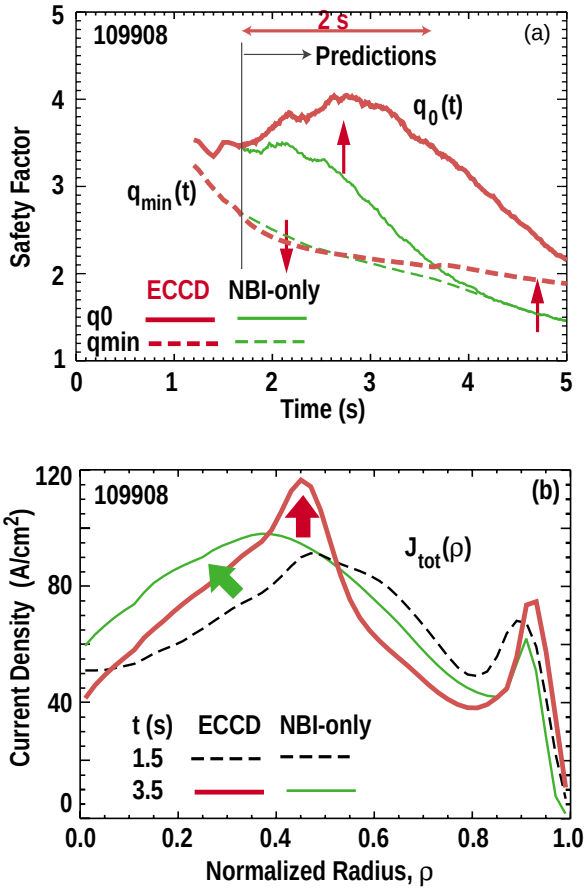

Murakami Figure 1

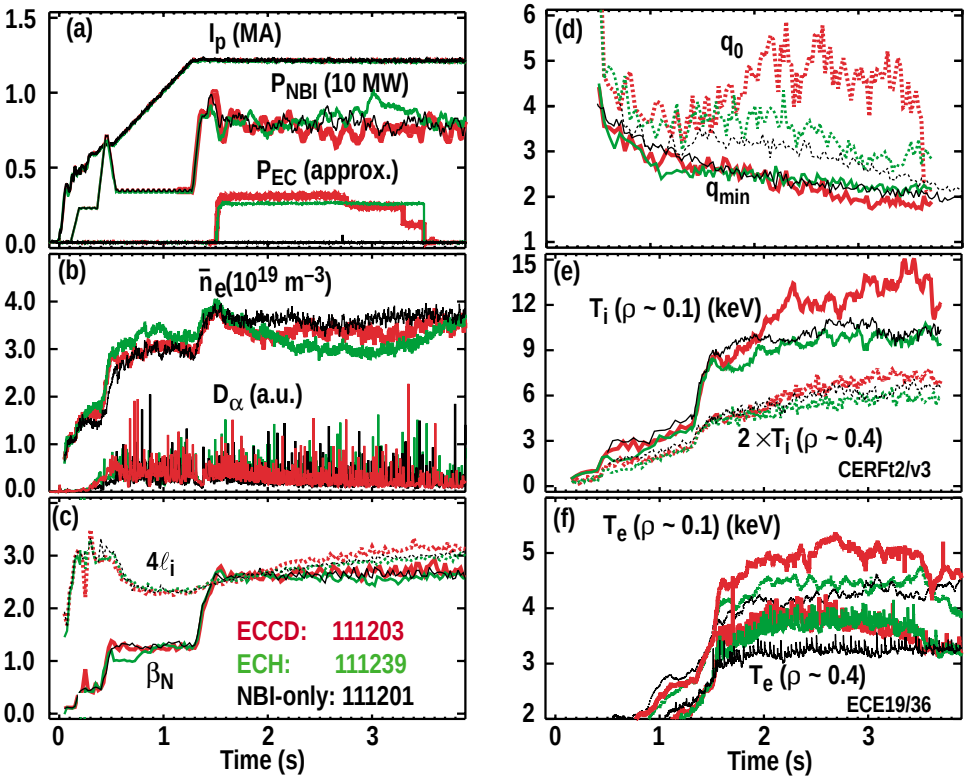

Murakami Figure 2

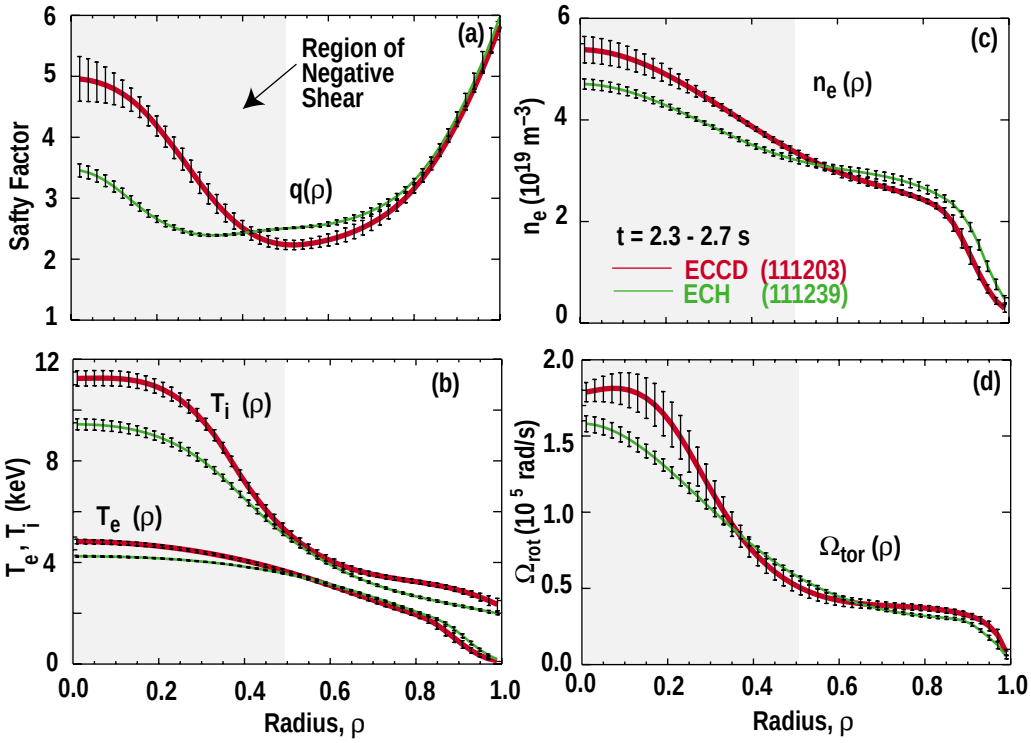

M. Murakami Figure 3

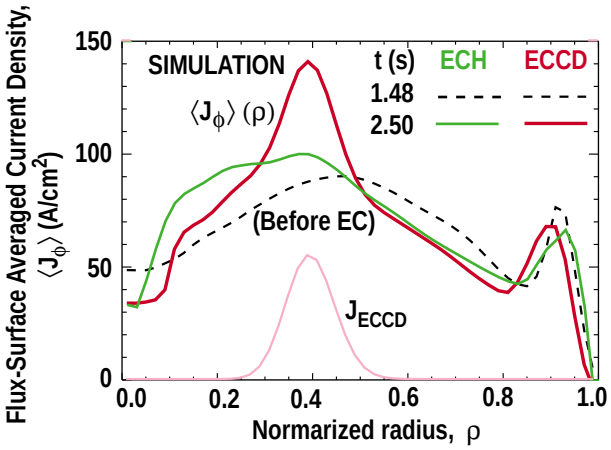

Murakami Figure 4

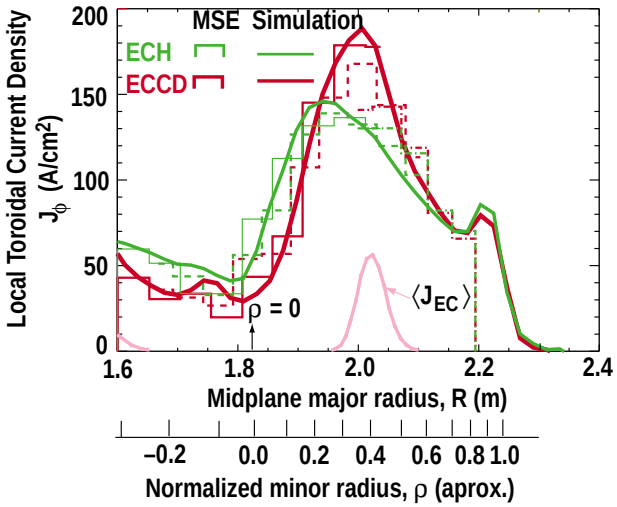

Murakami Figure 5

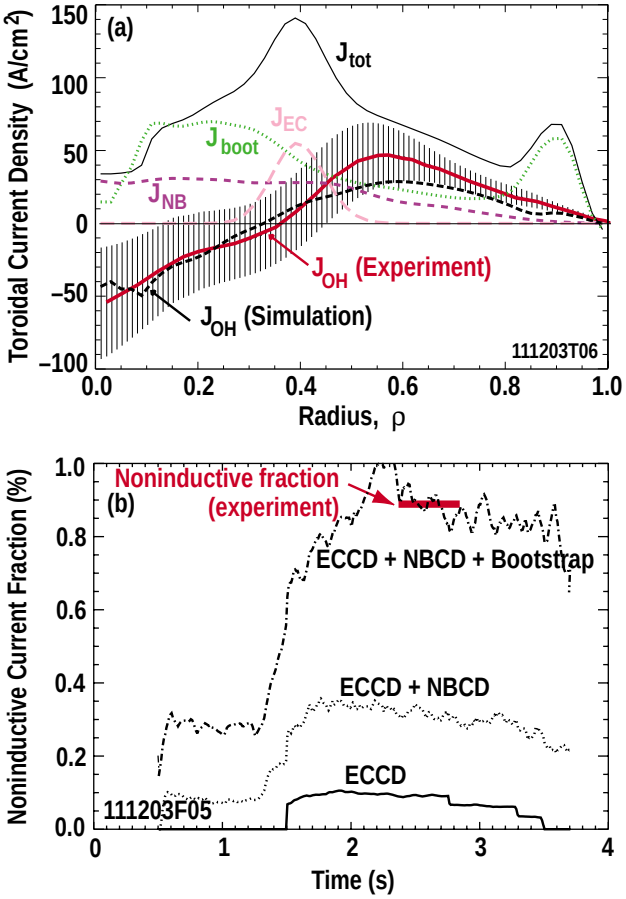

Murakami Figure 6

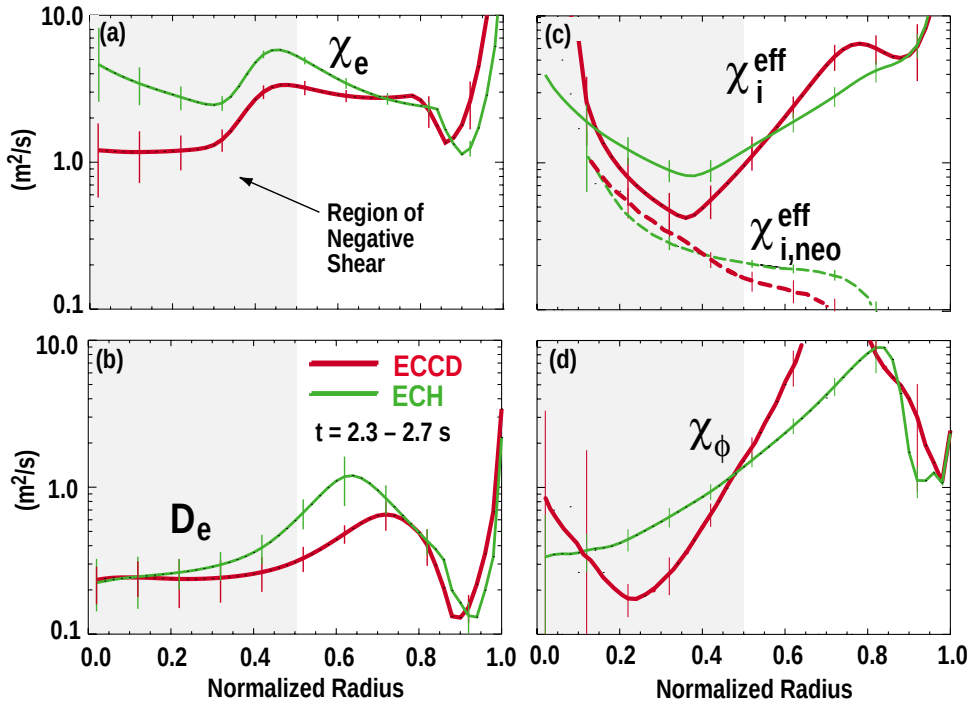

Murakami Figure 7

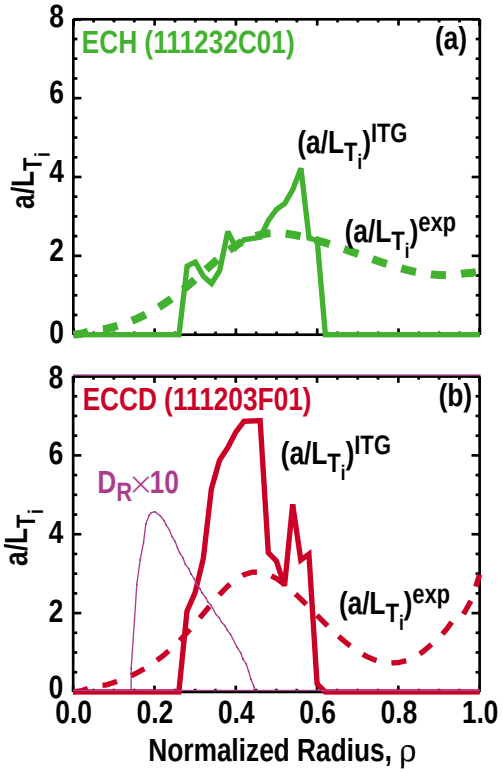

M. Murakami Figure 8

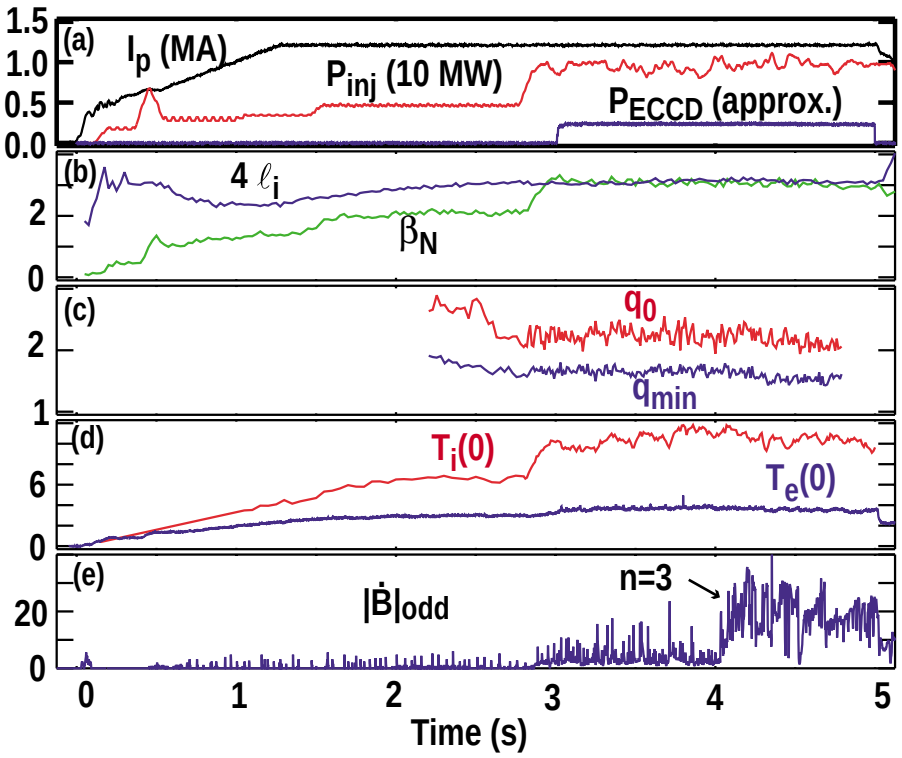

M. Murakami Figure 9

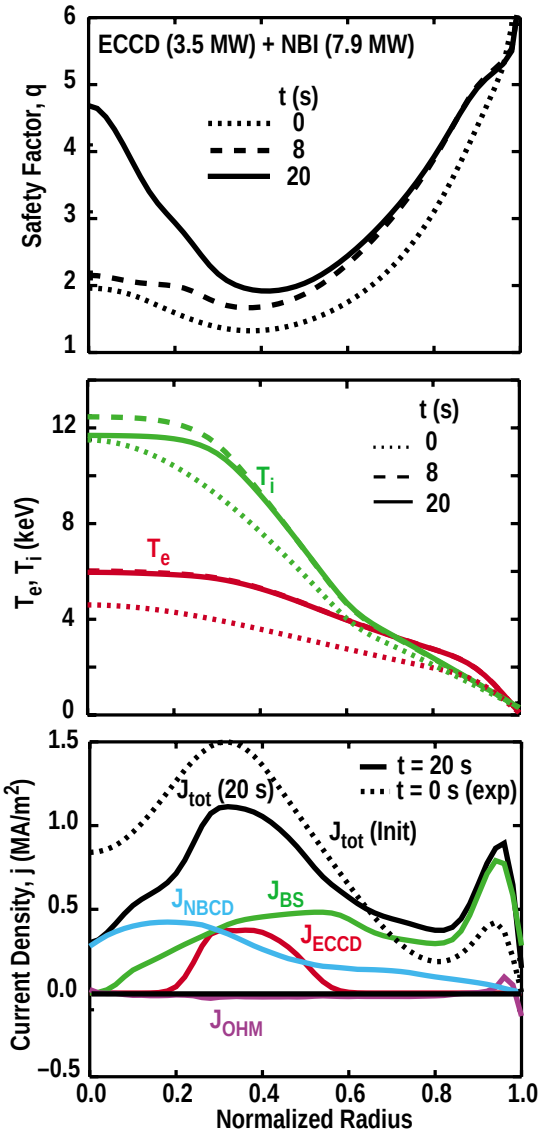

M. Murakami Figure 10

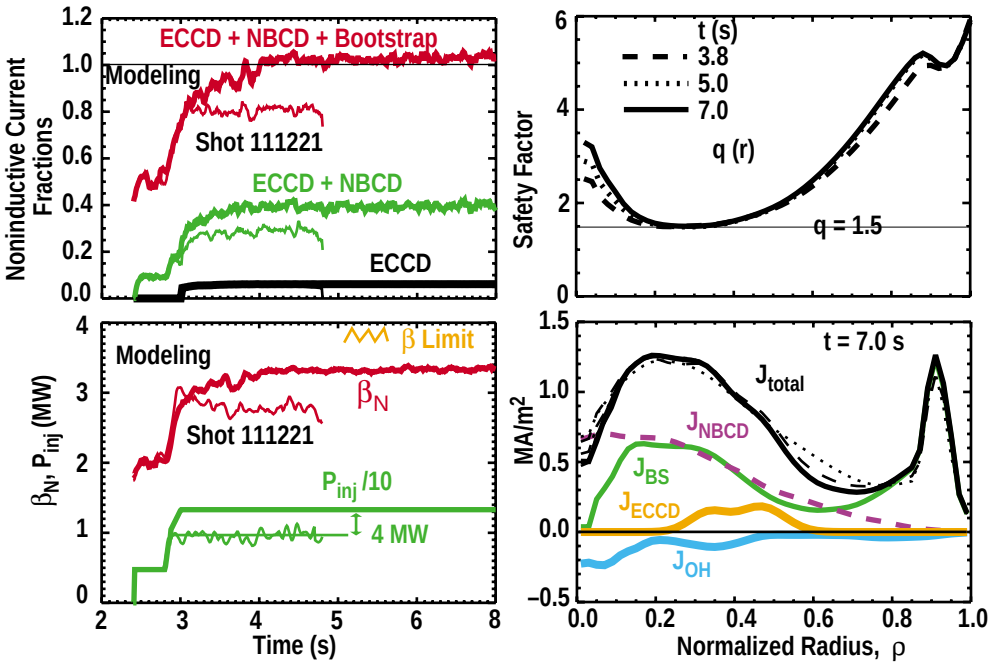

M. Murakami Figure 11